The Photodetector Array Camera & Spectrometer (PACS) for the Herschel Space Observatory

Albrecht Poglitsch[a], Christoffel Waelkens[b], Otto H. Bauer[a], Jordi Cepa[c], Thomas Henning[d], Chris van Hoof[e], Reinhard Katterloher[a], Franz Kerschbaum[f], Dietrich Lemke[d], Etienne Renotte[g], Louis Rodriguez[h], Pierre Royer[b], and Paolo Saraceno[i]

[a]Max-Planck-Institut f. extraterrestrische Physik, Postfach 1312, 85741 Garching, Germany
[b]Katholieke Universiteit Leuven, Celestijnenlaan 200B, 3001 Leuven, Belgium
[c]Instituto de Astrofisica de Canarias, C/Via Lactea s/n, La Laguna, 38200 Santa Cruz de Tenerife, Spain
[d]Max-Planck-Institut für Astronomie, Königstuhl 17, 69117 Heidelberg, Germany
[e]Interuniversity Microelectronics Center, Kapeldreef 75, 3001 Leuven, Belgium
[f]Institut für Astronomie der Universität Wien, Türkenschanzstraße 17, 1180 Wien, Austria
[g]Centre Spatial de Liège, Parc Scientifique du Sart Tilman, Avenue du Pré-Aily, 4031 Angleur-Liège, Belgium
[h]Commissariat à l'Energie Atomique, Service d'Astrophyisque, Orme des Merisiers, Bât. 709, 91191 Gif/Yvette, France
[i]Istituto di Fisica dello Spazio Interplanetario, Via del Fosso del Cavaliere, 00133 Roma, Italy

ABSTRACT

The Photodetector Array Camera and Spectrometer (PACS) is one of the three science instruments for ESA's far infrared and submillimetre observatory, Herschel. It employs two Ge:Ga photoconductor arrays (stressed and unstressed) with 16×25 pixels, each, and two filled Si bolometer arrays with 16×32 and 32×64 pixels, respectively, to perform imaging line spectroscopy and imaging photometry in the $57 - 210\mu$m wavelength band. In photometry mode, it will simultaneously image two bands, $60 - 85\mu$m or $85 - 130\mu$m and $130 - 210\mu$m, over a field of view of $\sim 1.75' \times 3.5'$, with full beam sampling in each band. In spectroscopy mode, it will image a field of $\sim 50'' \times 50''$, resolved into 5×5 pixels, with an instantaneous spectral coverage of ~ 1500km/s and a spectral resolution of $\sim 75 - 300$km/s. In both modes background-noise limited peformance is expected, with sensitivities (5σ in 1h) of ~ 3 mJy or $3 - 10 \times 10^{-18}$W/m^2, respectively.

Keywords: Instruments: far infrared - Instruments: space - Instruments: photometer, integral field spectrometer - Missions: Herschel

1. INTRODUCTION

The far infrared and submillimetre satellite Herschel will open up the wavelength range $60 - 600\mu$m to photometry and spectroscopy with unprecedented sensitivity and spatial resolution, unobscured by the Earth's atmosphere.

Within the complement of three instruments selected to form the science payload, the shortest wavelength band, $60 - 210\mu$m, will be covered by the Photodetector Array Camera & Spectrometer (PACS), which will provide both photometric and spectroscopic observing modes suited to address the key scientific topics of the Herschel mission.

In this paper we describe the design and the development status of PACS and give predictions on the expected in-orbit performance based on tests at subunit or instrument level of the PACS Qualification Model.

Further author information: (Send correspondence to A.P.)
A.P.: E-mail: alpog@mpe.mpg.de, Telephone: 49 89 30 000 3293

2. INSTRUMENT DESIGN

The requirements leading to the design of PACS have been discussed previously[1]; here we briefly summarize the instrument concept.

The instrument will offer two basic modes in the wavelength band $60-210\mu$m:

- Imaging dual-band photometry ($60-85$ or $85-130\mu$m and $130-210\mu$m) over a field of view of $1.75' \times 3.5'$, with full sampling of the telescope point spread function (diffraction/wavefront error limited)
- Integral-field line spectroscopy between 57 and 210 μm with a resolution of ~ 175 km/s and an instantaneous coverage of ~ 1500 km/s, over a field of view of $47'' \times 47''$

Both modes will allow spatially chopped observations by means of an instrument-internal chopper mirror with variable throw; this chopper also is used to alternatively switch two calibration sources into the field of view.

The focal plane sharing of the instrument channels is shown in Fig. 1.

The photometric bands, which can be observed simultaneously, cover the same field of view, while the field of view of the spectrometer is offset from the photometer field (Fig. 1). Since photometry and spectroscopy

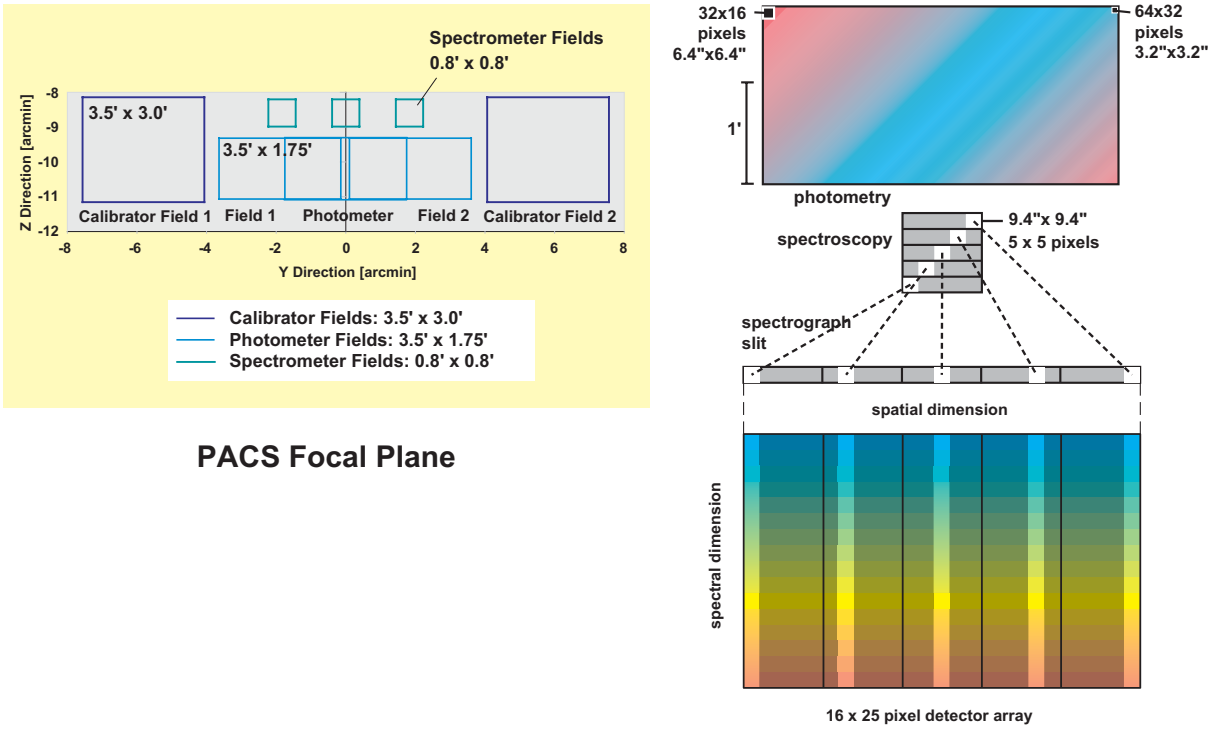

Figure 1. *Left: PACS focal plane usage. Long-wavelength and short-wavelength photometry bands cover identical fields of view. The spectrometer field of view is offset in the $+z$ direction. Chopping is done along the y axis (left-right in this view) and also allows observation of the internal calibrators on both sides of the used area in the telescope focal plane. The chopper throw for sky observations is $\pm 1/2$ the width of the photometer field such that object and reference fields can be completely separated (photometer field 1 and 2). Right: focal plane footprint. A fixed mirror is used to split the focal plane into the photometry and spectroscopy channels of the instrument. In the photometry section, the two wavelength bands are simultaneously imaged with different magnification to reach full beam sampling in both bands. In the spectroscopy section, an optical image slicer re-arranges the 2-dimensional field along the entrance slit of the grating spectrograph such that, for all spatial elements in the field, spectra are observed simultaneously.*

operation are mutually exclusive this has no effect on the observing efficiency. The focal plane unit provides these capabilities through five functional units:

- common input optics with the chopper, calibration sources and a focal plane splitter
- a photometer optical train with a dichroic beam splitter and separate re-imaging optics for the short-wavelength bands ($60-85\mu$m / $85-130\mu$m) and the long-wavelength band ($130-210\mu$m), respectively
- a spectrometer optical train with an image slicer unit for integral field spectroscopy, an anamorphic collimator, a diffraction grating in Littrow mount with associated actuator and position readout, anamorphic re-imaging optics, and a dichroic beam splitter for separation of diffraction orders
- 2 bolometer arrays with cryogenic buffers/multiplexers and a common 0.3 K sorption cooler
- 2 photoconductor arrays with attached cryogenic readout electronics (CRE)

2.1. Photoconductor Arrays

The 25×16 pixels Ge:Ga photoconductor arrays (Fig. 2) are a completely modular design. 25 linear modules of 16 pixels each are stacked together to form a contiguous, 2-dimensional array. For the long-wavelength band a sophisticated stressing mechanism ensures a homogeneous stress within each pixel along the entire stack of 16. The second – "unstressed" – array with improved short-wavelength responsivity is almost identical to the long-wavelength array, except for the mechanical stress on the pixels which is reduced to about 10% of the level needed for the long-wavelength response. Details of the design of both arrays have been published.[2–5]

A close-up of one linear, high-stress detector module is shown in Fig. 2 (top right) with the light cones removed. The light cones in front of the actual detector block provide for area-filling light collection in the focal plane and feed the light into the individual integrating cavities around each individual, mechanically stressed detector crystal. The light cones also act as a very efficient means of straylight suppression because their solid angle of acceptance is matched to the re-imaging optics such that out-of-beam light is rejected. Responsivity measurements of both stressed and unstressed modules show sufficiently homogeneous spectral and photometric response within each module (Fig. 2, bottom center). Absolute responsivity numbers are preliminary as the optimum bias for in-orbit operation is not determined, yet. Likely numbers will be $\sim$ 8A/W for the unstressed detectors and $\sim$30A/W for the stressed detectors.

Each linear module of 16 detectors is read out by a cryogenic amplifier/multiplexer circuit in CMOS technology[6,7] (Fig. 2, center right). The circuit integrates 18 capacitive-feedback transimpedance amplifiers (CTIA) with switchable capacitors – to ensure flexibility in terms of infrared background and readout rate – and sample-and-hold output stages with a multiplexing output buffer. The readout electronics is integrated into the detector modules. The relatively high telescope background (compared to e.g. ISO or Spitzer) and the readout noise spectrum require a rapid readout (1/256 s) of each pixel which leads to a raw data rate substantially above the maximum rate allowed by the Herschel on-board data handling system. A combination of data reduction and lossless data compression[8,9] is carried out by a dedicated Signal Processing Unit (SPU) within the PACS warm electronics. The data reduction part is implemented as either sub-ramp fitting or binning of n samples along the integration ramp. In either case, the lossless compression allows a data rate of 64 samples/s within the available telemetry bandwidth.

2.2. Bolometer Arrays

The PACS bolometers are filled arrays of square pixels which allow instantaneous beam sampling. Fig. 3 (top right) shows a cut-out of the 64×32 pixels bolometer array assembly. 4×2 monolithic sub-arrays of 16×16 pixels are tiled together to form the short-wave focal plane array (Fig. 3, top center). In a similar way, 2 sub-arrays of 16×16 pixels are tiled together to form the long-wave focal plane array. Fig. 3 (top left) shows a development model of the 16×16 subarray with a micrograph of one pixel. The subarrays are mounted on a 0.3 K carrier which is thermally isolated from the surrounding 2 K structure. The buffer/multiplexer electronics is split in two levels; a first stage is part of the indium-bump bonded back plane of the focal plane arrays, operating at 0.3 K. Ribbon cables connect the output of the 0.3 K readout to a buffer stage running at 2 K (Fig. 3, top center). Details

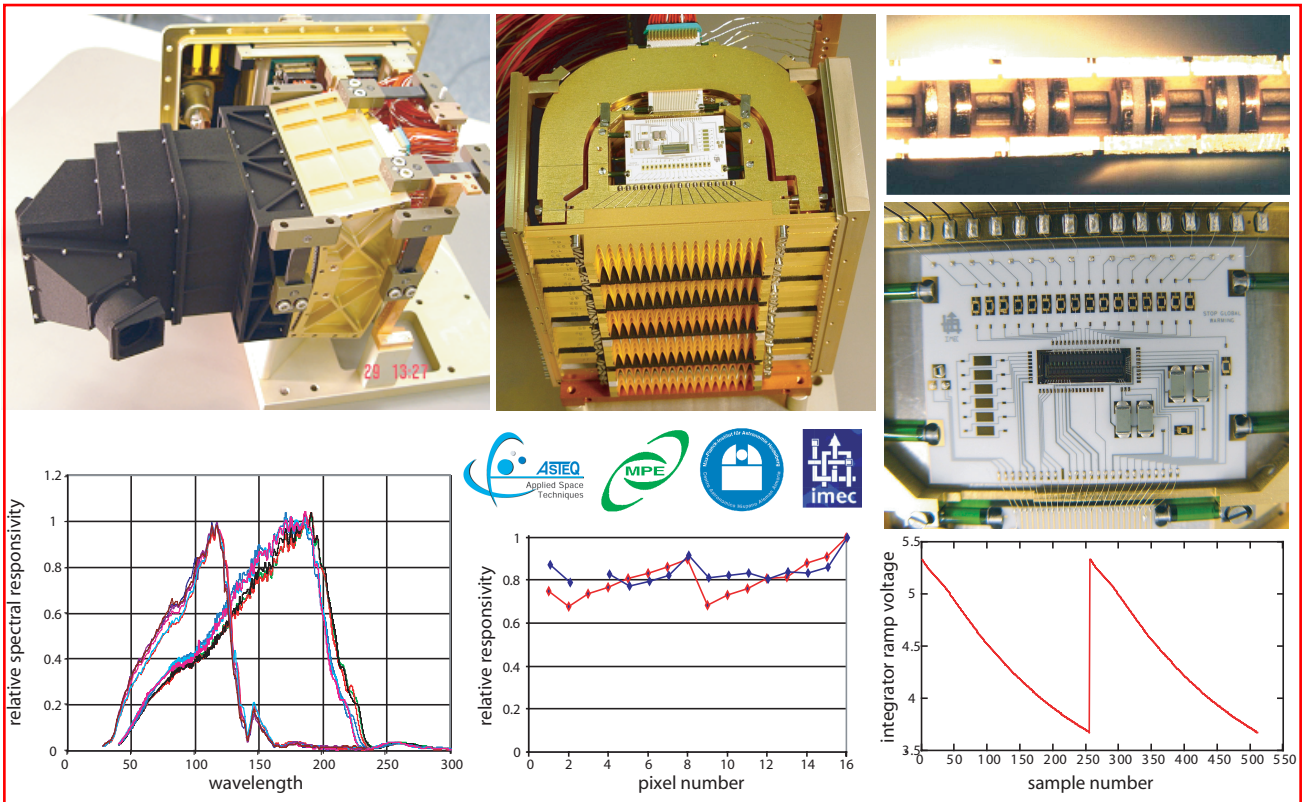

Figure 2. *Top left: Fully assembled* 25×16 *stressed Ge:Ga photoconductor array (QM), with baffle, housing, and electrical distribution/filter board. Top center: The 25 stressed modules integrated into their housing. Stress is applied to the whole stack of 16 Ge crystals and separating pressure "pistons" in each module with a precision screw; the C-shaped part of the module serves as a spring clamp. Light cones provide for area-filling light collection onto the individual detectors. Top right: Close-ups of one linear 16-element detector module without light cones (upper panel) and of the front-end electronics with the CRE chip which provides an integrating amplifier for each pixel and an output muliplexer (lower panel). Bottom left: Relative spectral response of stressed (long wavelength) and unstressed(short wavelength) detectors. Bottom center: Relative photometric response of pixels within modules. Bottom right: Integration ramps of one channel as measured at the CRE multiplexer output.*

on the bolometer design are given elsewhere.[10,11] The post-detection bandwidth (thermal /electrical) of the bolometers is ∼5 Hz; the 1/f "knee" of the bolometer/readout system has been measured to occur below 0.1 Hz. The multiplexing readout samples each pixel at a rate of 40 Hz or 20 Hz. Both array assemblies are mounted in a subunit of the FPU together with the 0.3 K cooler (Fig. 3, bottom left) which provides uninterrupted operation for two days. This cooler is nearly identical to the unit developed for SPIRE.[12] Measurements on a 16×16 subarray (Fig. 3), bottom center/right) show homogeneous responsivity across the array at a sufficiently high level to overcome the demonstrated electronic readout noise under PACS/Herschel background loads. Because of the large number of pixels, data compression by the SPU is required. The raw data are binned to an effective 10 Hz sampling rate (adequate for a 5 Hz detector bandwith); after that, the same lossless compression algorithm is applied as with the spectrometer data.

2.3. Entrance Optics, Chopper and Calibrators

The entrance optics (see Fig. 4) fulfills the following tasks: It creates an image of the telescope secondary mirror (the entrance pupil of the telescope) on the focal plane chopper; this allows spatial chopping with as little as possible modulation in the background received by the instrument. It also provides for an intermediate pupil position where the Lyot stop and the first blocking filter, common to all instrument channels, can be positioned,

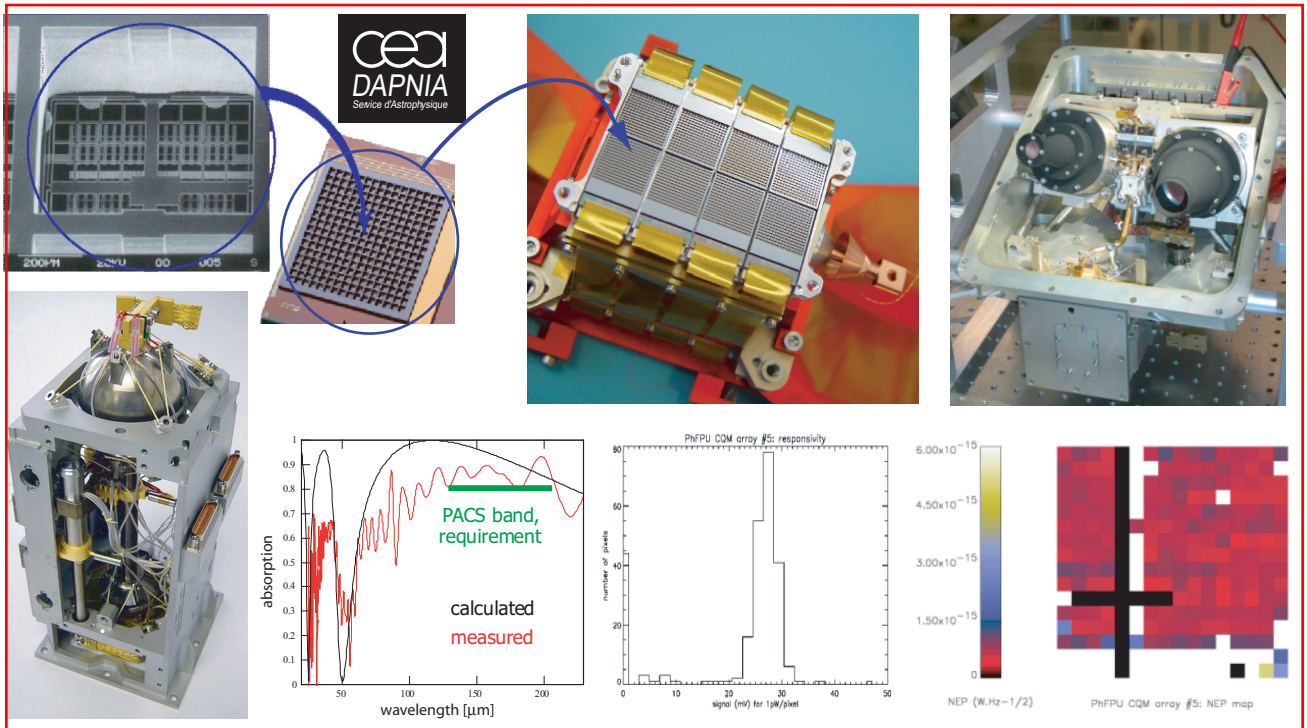

Figure 3. *Top left: Micrograph of one pixel of the filled bolometer array development model next to a photo of the* 16×16 *pixels subarray. The physical size of a PACS pixel is 0.75 mm. The absorber and back-reflector grids as well as the integrated thermistor are monolithic silicon structures. Top center:* 4×2 *subarrays form the focal plane of the short-wave bolometer assembly. The 0.3K multiplexers are bonded to the back of the subarrays. Ribbon cables lead to the 2 K buffer electronics. Top right: Photometer focal plane unit (QM) with the two bolometer assemblies (short-wave/long-wave) and the 0.3 K sorption cooler. Bottom left: The 0.3 K* ^{3}*He sorption cooler with evaporator, sorption pump, connecting tube, and heat switches. All functional components are suspended from the (4 K) structural frame by Kevlar strings. Bottom center-left: Efficiency of the bolometer absorber structure in the PACS long-wavelength band. Bottom center-right: Responsivity histogram of one* 16×16 *QM subarray. Bottom right: NEP map of the same subarray.*

and it allows the chopper – through two field mirrors adjacent to the used field of view in the telescope focal surface – to switch between a (chopped) field of view on the sky and two calibration sources (see also Fig. 1).

The chopped image is then re-imaged onto an intermediate focus where a fixed field mirror splits off the light into the spectroscopy channel. The remaining part of the field of view passes into the photometry channels. A "footprint" of the focal-plane splitter is shown in Fig. 1.

The calibration sources are placed at the entrance to the instrument to have the same light path for observation and internal calibration. This is essential for removing baseline ripples as best as possible, a serious task with a warm telescope and the associated high thermal background. To eliminate non-linearity or memory problems with the detector/readout system, the calibrator sources are gray-body sources providing FIR radiation loads slightly above or below the telescope background, respectively. This is achieved by diluting the radiation from a (small) black source with a temperature near the telescope temperature inside a cold diffusor sphere with a (larger) exit aperture. The temperature of the radiator (~ 80 K) is stabilized within a few mK.

The chopper (Fig. 5, left) provides a maximum throw of $4'$ on the sky; this allows full separation of an "object" field and a "reference" field. The chopper[13,14] is capable of following arbitrary waveforms with a resolution of $1''$, referred to the sky, and delivers a duty-cycle of $\sim$90% at a chop frequency of 5 Hz.

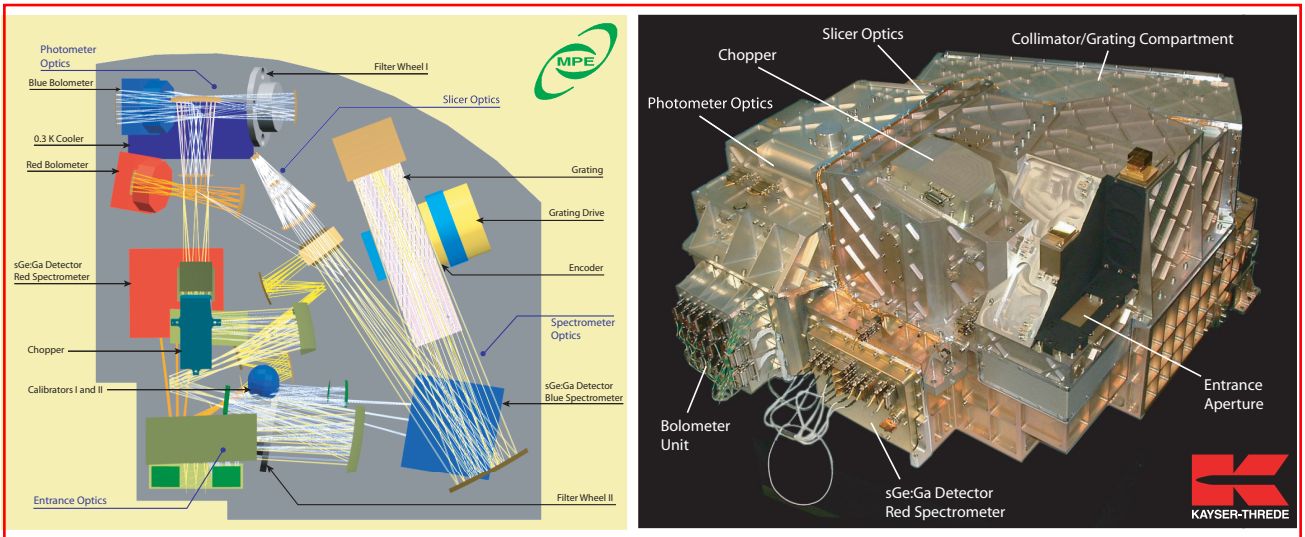

Figure 4. *PACS Focal Plane Unit. Left: Optical layout. After the common entrance optics with calibrators and the chopper, the field is split into the spectrometer train and the photometer trains where a dichroic beam splitter feeds separate re-imaging optics for the two bolometer arrays. In the spectrometer train, the image slicer converts the square field into an effective long slit for the Littrow-mounted grating spectrograph. The dispersed light is distributed to the two photoconductor arrays by a dichroic beam splitter which acts as an order sorter for the grating. Right: Fully assembled Qualification Model.*

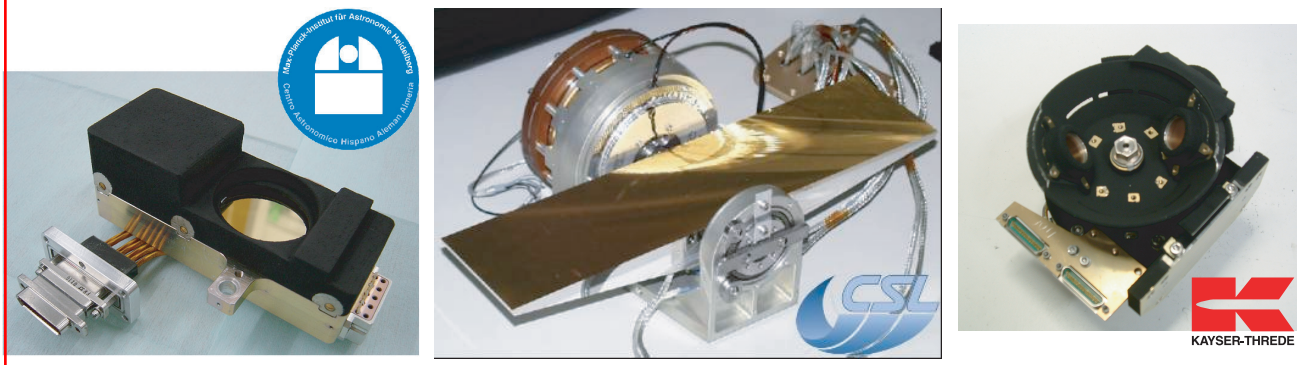

Figure 5. *PACS cryomechanisms. Left: Qualification Model of the focal plane chopper.*[13, 14] *The chopper is used for sky modulation and also to deflect the detector field of view toward 2 internal calibration sources. Center: Qualification Model of the grating unit. A torquer motor is used to actuate the grating angle which is measured with sub-arcsecond precision by an Inductosyn angular resolver. Right: Qualification Model of one of the two filter wheels. The motor is the same design as the grating torquer.*

2.4. Imaging Photometer

After the intermediate focus provided by the entrance optics, the light is split into the long-wavelength and short-wavelength channels by a dichroic beamsplitter with a transition wavelength of 130μm and is re-imaged with different magnification onto the respective bolometer arrays.

The 32×16 or 64×32 pixels in each array are used to image a field of view of $3.5' \times 1.75'$ in both channels, providing full beam sampling at 90μm and 180μm, respectively. The long-wavelength band ($130 - 210\mu$m) can be combined with either one of the two bands of the short-wavelength channel, $60 - 85\mu$m or $85 - 130\mu$m. The two short-wavelength bands are selected by two filters with a filter wheel (Fig. 5, right). All filters are implemented

as multi-mesh filters and provided by Cardiff University*.

The re-imaging optics also creates exit pupils at appropriate distances from the bolometer arrays to allow efficient baffling with the bolometer assemblies.

2.5. The Integral-Field Spectrometer

The spectrometer covers the wavelength range from 57μm to 210μm. It provides a resolving power of $1000-4000$ (Δv $= 75-300$km/s) with an instantaneous coverage of ~ 1500km/s and simultaneous imaging of a $47'' \times 47''$ field of view, resolved into 5×5 pixels. An image slicer employing reflective optics is used to re-arrange the 2-dimensional field of view along a 1×25 pixels entrance slit for a grating spectrometer, as schematically shown in Fig. 1. A detailed description of the slicer optics is given in a paper on the SOFIA experiment FIFI LS.[15]

The integral-field concept has been selected because simultaneous spectral and spatial multiplexing allows the most efficient detection of weak individual spectral lines with sufficient baseline coverage and high tolerance to pointing errors without compromising spatial resolution, as well as for spectral line mapping of extended sources regardless of their intrinsic velocity structure.

The Littrow-mounted grating with a length of $\sim$ 30cm is operated in 1$^{\rm st}$, 2$^{\rm nd}$ or 3$^{\rm rd}$ order, respectively, to cover the full wavelength range. The 1$^{\rm st}$ order covers the range $105-210\mu$m, the 2$^{\rm nd}$ order $72-105\mu$m, and the 3$^{\rm rd}$ order $57-72\mu$m. Anamorphic collimating optics expands the beam to an elliptical cross section to illuminate the grating over a length required to reach the desired spectral resolution. The grating is actuated by a cryogenic motor[16] (Fig. 5, center) with arcsec precision which allows spectral scanning/stepping for improved spectral flatfielding and for coverage of extended wavelength ranges. The settling time for small motions is $\leq$ 50ms.

The light from the 1$^{\rm st}$ diffraction order vs. light from the other two orders is separated by a dichroic beam splitter and passed on into two optical trains feeding the respective detector array (stressed/unstressed) for the wavelength ranges $105-210\mu$m and $57-105\mu$m. Anamorphic re-imaging optics is employed to independently match the spatial and spectral resolution of the system to the square pixels of the detector arrays. The filter wheel (Fig. 5, right) in the short-wavelength path selects the 2$^{\rm nd}$ or 3$^{\rm rd}$ grating order.

3. OBSERVING MODES

The observing modes supported by PACS are combinations of *instrument modes* and *satellite pointing modes*. All satellite pointing modes – stare, raster, and line scan (with or without nodding) – are foreseen to be used for PACS observations. The following section describes the PACS instrument modes.

3.1. Dual-band Photometry

In this mode, both bolometer arrays are operating, providing full spatial sampling in each band. The long-wave array images the $130-210\mu$m band while the short-wave array images either the $60-85\mu$m or the $85-130\mu$m band. The respective sub-band is selected by a filter. This mode is the standard mode for PACS as prime instrument. Observing parameters are the chopper mode (off/on; waveform, throw), pointing parameters (stare/raster/scan;nod), and the integration time per pointing.

3.2. Single-band Photometry

In this mode, only one bolometer array is operating such that either the long-wave array images the $130-210\mu$m band or short-wave array images the $60-85\mu$m or the $85-130\mu$m band. This mode serves as a test mode for PACS as prime instrument, but it is also foreseen as standard mode for PACS/SPIRE parallel observations. Observing parameters are the chopper mode (off/on; waveform, throw), pointing parameters (stare/raster/scan;nod), and the integration time per pointing.

*P.A.R. Ade, Department of Physics and Astronomy, University of Wales, Cardiff, UK

3.3. Line Spectroscopy

In this mode, one or two photoconductor arrays are operating for observations of individual lines. The long-wave array will observe in the $105 - 210\mu$m band while the short-wave array observes in the $57 - 72\mu$m or $72 - 105\mu$m band. The wavelength in the primary band automatically determines the wavelength in secondary band; therefore, for most practical purposes, one can assume that only one line can be observed at a time, and only one array needs to be read out. This will help to reduce the integrated data rate. Observing parameters are the scan width (default 0), the chopper mode (off/on; waveform, throw), pointing parameters (stare/raster/scan;nod), and the integration time per pointing.

3.4. Range Spectroscopy

In this mode, both photoconductor arrays are operating for effective observations of extended wavelength ranges. Such observations can be continuous scans with full spectral resolution or steps for a coarser sampling of, e.g., spectral energy distributions (SEDs). The long-wave array will observe in the $105-210\mu$m band while the short-wave array observes in the $57-72$ or $72-105\mu$m band. Observing parameters are the start- and end wavelength, the resolution mode, the chopper mode (off/on; waveform, throw), pointing parameters (stare/raster/scan;nod), and the integration time per pointing.

4. SYSTEM PERFORMANCE

Based on the present knowledge of the components of PACS and of the Herschel satellite, the performance of the entire system can be estimated in terms of what the observer is concerned with, i.e., an assessment of what kind of observations will be feasible with Herschel/PACS, and how much observing time they will require.

The system sensitivity of the instrument at the telescope depends mainly on the optical efficiency, i.e. the fraction of light from an astronomical source arriving at the telescope that actually reaches the detector, and on the thermal background radiation from the telescope or from within the instrument as long as the fluctuations of the background constitute the dominant noise source. As will be shown below, background-noise limited performance should be feasible in both spectroscopy and photometry modes with the PACS detectors.

4.1. Optical Efficiency

The system optical efficiency has been modeled to the following level of detail:

- *Telescope efficiency:* The fraction of the power of a point source in the central peak of the point spread function is modeled in terms of absorption/obstruction, diffraction, and geometrical wave front errors (6μm r.m.s.), which have been assumed to occur as spherical aberration.
- *Chopper:* Errors/jitter in the chopper throw and the duty cycle ($> 80\%$) are considered.
- *Mirrors and filters:* scatter/absorption losses – excluding diffraction – on each reflection by a mirror (1%) and efficiencies of filters/dichroics (as measured for the QM filters) are taken into account.
- *Diffraction:* An end-to-end diffraction analysis with the physical optics package GLAD 4.5 has been carried out for the spectrometer, where the image slicer is the most critical element of the PACS optics,[15, 17] and a simplified analysis for the less critical photometer as well as the effect of diffraction/vignetting by the entrance field stop and Lyot stop have been included.
- *Grating efficiency:* The grating has been analysed and optimised with a full electromagnetic code.[17]

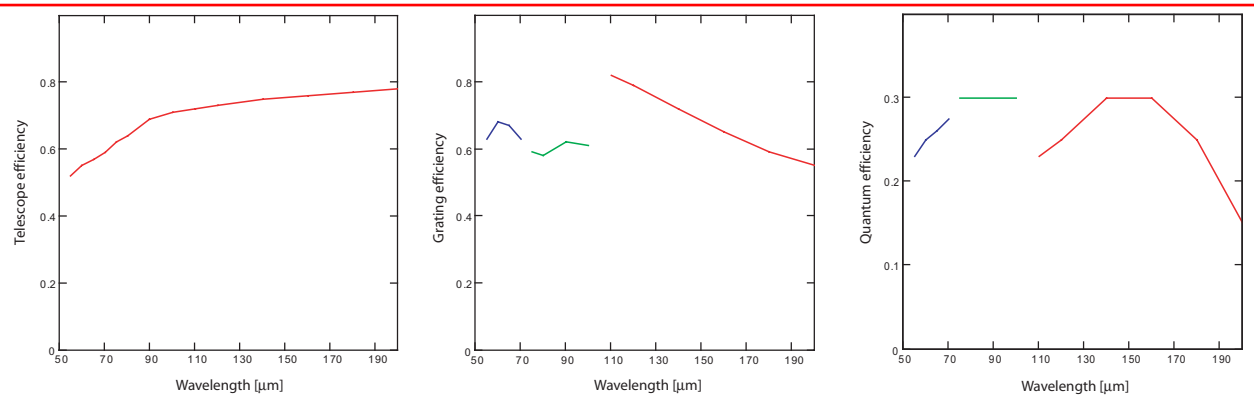

Figure 6. *Optical efficiencies. Left: Telescope (main beam) efficency for an assumed wave front error of 6μm r.m.s. Center: Calculated grating efficiency. Right: Predicted photoconductor quantum efficiency based on typical relative spectral responsivity measurements, normalized to a (single point) absolute determination of quantum efficiency from a signal-to-noise measurement of a high-stress module with a TIA readout under well-defined background conditions near the peak responsivity.*

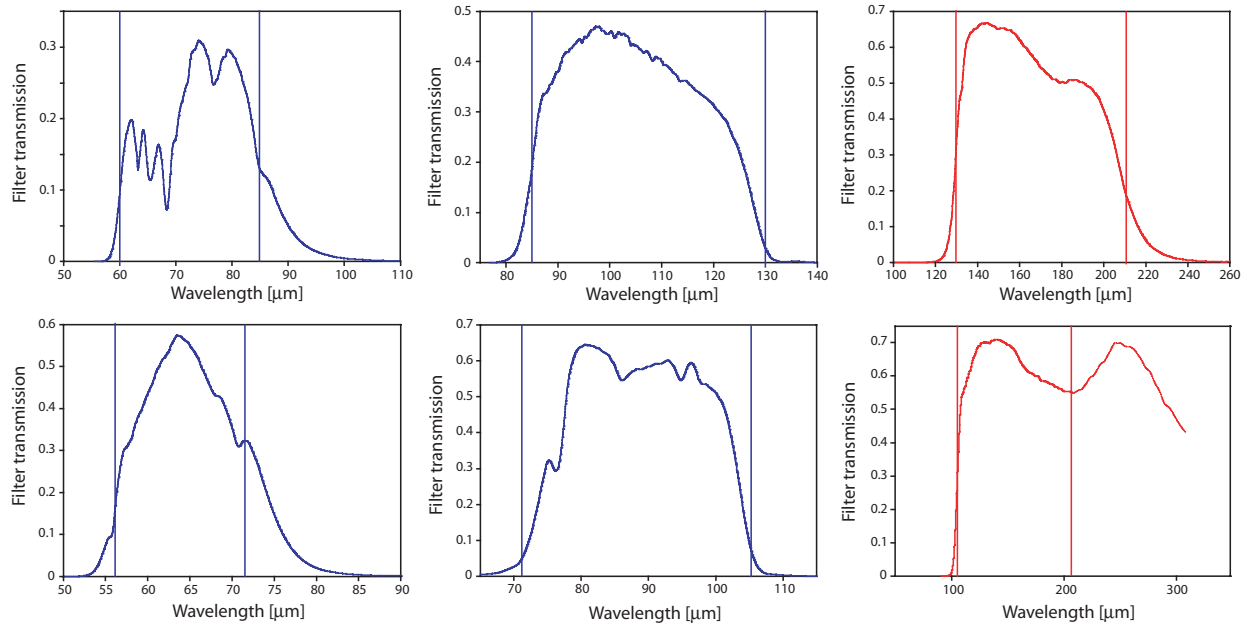

Figure 7. *Filter transmission of the QM filters. The graphs represent the overall transmission of the combined filters in each branch of the instrument. The nominal band limits are indicated by the vertical lines. Top left: $60-85\mu m$ photometer band. Top center: $85-130\mu m$ photometer band. Top right: $130-210\mu m$ band. Bottom left: $57-72\mu m$ spectrometer band. Bottom center: $72-105\mu m$ spectrometer band. Bottom right: $105-210\mu m$ spectrometer band. Note: the low transmission at the shortest wavelengths is mainly due to a problem with the dichroic beam splitters which will be improved for the FM.*

4.2. Detectors

The projected (dark) detector NEP of the Ge:Ga photoconductor system is $\leq 5 \times 10^{-18}$ W Hz$^{-1/2}$ for the stressed detectors and $\leq 1 \ldots 2 \times 10^{-17}$ W Hz$^{-1/2}$ for the unstressed detectors; it is dominated by the noise of the Cryogenic Readout Electronics which – with the most recent, post-QM CRE generation – is near spec for the stressed detectors because of their higher responsivity, but a factor $2 \ldots 3$ too high for the unstressed detectors. A new circuit is presently being developed for the FM detectors to meet the requirements for background-noise limited

performance. Detective quantum efficiencies of $\sim$ 30% are feasible with careful cavity design.[18] Our measurements of the fully stressed PACS modules with a TIA laboratory readout system even indicate a quantum efficiency near 35%. The achievable in-orbit performance depends critically on the effects of cosmic rays, in particular, high-energy protons. We have performed first proton irradiation tests at the synchrotron source of the Université Catholique de Louvain (Louvain la Neuve, Belgium) on a stressed QM detector module under reasonably realistic conditions in terms of proton flux and energy, FIR background, and metallic shielding by the cryostat. A preliminary analysis of the results indicates that we will face a permanently changing detector responsivity: cosmic ray hits lead to an instantaneous increase in responsivity, followed by a curing process due to the thermal IR background radiation. The necessary operating parameters (in particular, integration ramp length, detector bias, and chopping schemes) still need to be explored before a dependable prediction can be made to which level the cosmic ray effects can be modelled and eliminated, or at what level they will add to the effective detector noise.

For the bolometers, the calculated background noise from the telescope is $\sim 2 \times 10^{-16}$ W Hz$^{-1/2}$. To ensure background-limited performance we require an electrical NEP of $\leq 10^{-16}$ W Hz$^{-1/2}$ which has been demonstrated on a 16×16 bolometer subarray of the QM detector production run with its 0.3K multiplexer. The 2K buffer amplifier has been demonstrated separately. The calculated and measured absorption efficiency (equivalent to the detective quantum efficiency) is >80%.

4.3. Image Quality and Beam Sampling

The photometer optics – by design – delivers diffraction-limited image quality (Strehl ratio $\geq$95%). This has been verified by visible-optical measurements of the (geometrical) spot sizes as part of the FPU alignment procedure. We therefore assume that the instrument optics will only contribute in a negilible way to the dilution of the central peak of the telescope PSF. This assumption will be verified durimg the QM instrument level tests with a telescope simulator which allows observations of artificial sky masks.

The concept of approximately full beam sampling with our (filled) array will distribute the flux of a point source over several pixels. An equivalent dilution applies to the background received by the pixel. To recover the total flux (in the central peak of the PSF) several pixels have to be co-added. For the calculation of the system sensitivity this is taken into account through a pixel efficiency factor, which is defined as the fraction of the pixel area to the PSF area.

The spectrometer, and in particular its image slicer, is used over a large wavelength range. The (spatial) pixel scale is a compromise between resolution at short wavelengths and observing efficiency (mapped area) at long wavelengths. Full spatial sampling will require a fine raster with the satellite, for spectral line maps with full spatial resolution. For the sensitivity calculation this is neglected as the line flux will always be collected with the filled detector array. Therefore, for the plain detection of a line source, one pointing is sufficient. Fully resolved maps will require between 2 and 8 raster pointings, between the long and short wavelength end of the spectrometer range, with correspondingly longer integration time.

The spectral sampling also varies within each grating order; detection to the instantaneous resolution as given by the convolution of the diffraction-limited resolution with the pixel function is the default for the sensitivity estimates.

4.4. System Sensitivity

For the calculation of the system sensitivity we have included our present best knowledge of all components in the detection path as described above. The results for photometry and spectroscopy are shown in Fig. 8

It needs to be stressed that these figures must be considered preliminary, given the early state of the test program carried at the time of this writing. In some areas (e.g. short wavelength filters) we foresee improvement for the FM compared to the achieved performance used in the system model, in other areas (in particular, the cryogenic readout electronics for the photoconductor arrays) we have already assumed better performance than what has been demonstrated so far. A more reliable prediction will be possible after characterization of some of the critical FM components/subunits, in combination with the results from the ongoing QM instrument level tests.

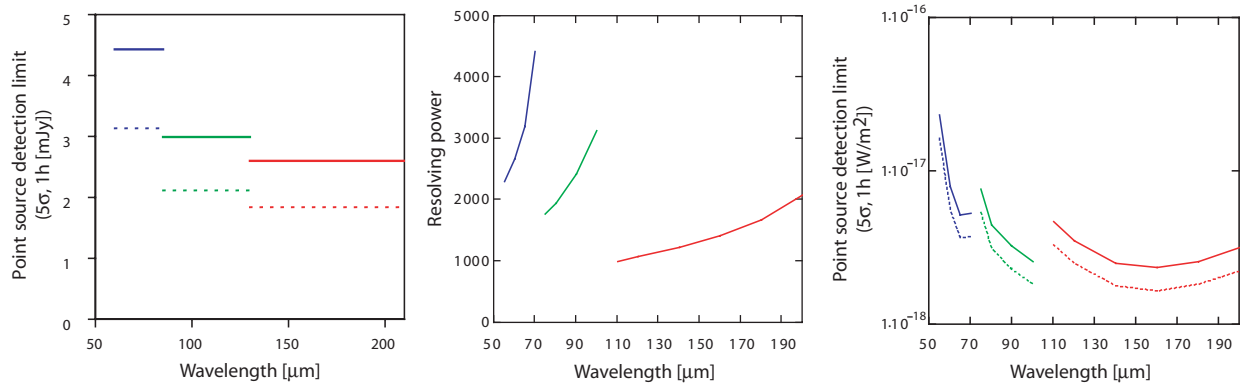

Figure 8. *Sensitivity of the PACS instrument on Herschel for point source detection in photometry mode (left) and spectroscopy mode (right). For spectroscopy we assume that the astronomical line is unresolved at the respective resolving power of the instrument (center). The solid lines represent chopped observations where only half of the integration time is spent on the source. The dashed lines represent modulation techniques like on-array chopping or line scans where all the integration time is spent on the source.*

ACKNOWLEDGMENTS

This work is supported by the following funding agencies: ASI (Italy), BMVIT (Austria), CEA/CNES (France), DLR (Germany), ESA-PRODEX (Belgium), and CDT (Spain).

REFERENCES

1. A. Poglitsch, C. Waelkens, and N. Geis in *IR Space Telescopes and Instruments*, J. Mather, ed., *Proc. SPIE* **4850**, pp. 662–673, 2003.
2. S. Kraft, O. Frenzl, O. Charlier, T. Cronje, R. O. Katterloher, D. Rosenthal, U. Groezinger, and J. W. Beeman in *UV, Optical, and IR Space Telescopes and Instruments*, J. B. Breckinridge and P. Jakobsen, eds., *Proc. SPIE* **4013**, pp. 233–243, 2000.
3. S. Kraft, P. Merken, Y. Creten, J. Putzeys, C. van Hoof, R. O. Katterloher, D. Rosenthal, M. Rumitz, U. Groezinger, R. Hofferbert, and J. W. Beeman in *Sensors, Systems, and Next-Generation Satellites V*, H. Fujisada, J. B. Lurie, and K. Weber, eds., *Proc. SPIE* **4540**, pp. 374–385, 2001.
4. D. Rosenthal, J. W. Beeman, N. Geis, U. Groezinger, R. Hoenle, R. O. Katterloher, S. Kraft, L. W. Looney, A. Poglitsch, W. Raab, and H. Richter in *Proceedings FIR, Submm & mm Detector Technology Workshop*, J. Wolf, J. Farhoomand, and C. McCreight, eds., *NASA/CP-* **211408**, 2002.
5. A. Poglitsch, R. Katterloher, R. Hoenle, J. Beeman, E. Haller, H. Richter, U. Groezinger, N. Haegel, and A. Krabbe in *Millimeter and Submillimeter Detectors for Astronomy*, T. Phillips and J. Zmuidzinas, eds., *Proc. SPIE* **4855**, pp. 115–128, 2003.
6. O. Charlier in *UV, Optical, and IR Space Telescopes and Instruments*, J. B. Breckinridge and P. Jakobsen, eds., *Proc. SPIE* **4013**, pp. 325–332, 2000.
7. Y. Creten, P. Merken, J. Putzeys, and C. van Hoof in *Proceedings FIR, Submm & mm Detector Technology Workshop*, J. Wolf, J. Farhoomand, and C. R. McCreight, eds., *NASA/CP-* **211408**, 2002.
8. H. Bischof, A. Belbachir, D. Hoenigmann, and F. Kerschbaum in *UV, Optical, and IR Space Telescopes and Instruments*, J. B. Breckinridge and P. Jakobsen, eds., *Proc. SPIE* **4013**, pp. 244–252, 2000.
9. F. Kerschbaum, H. Bischof, A. N. Belbachir, T. Lebzelter, and D. Hoenigmann in *UV, Optical, and IR Space Telescopes and Instruments*, J. B. Breckinridge and P. Jakobsen, eds., *Proc. SPIE* **4013**, pp. 253–262, 2000.
10. P. Agnese, C. Buzzi, P. Rey, L. Rodriguez, and J.-L. Tissot in *Infrared Technology and Applications XXV*, B. F. Andresen and M. S. Scholl, eds., *Proc. SPIE* **3698**, pp. 284–290, 1999.

11. P. Agnese, C. Cigna, J.-L. Pornin, R. Accomo, C. Bonnin, N. Colombel, M. Delcourt, E. Doumayrou, J. Lepennec, J. Martignac, V. Reveret, L. Rodriguez, and L. Vigroux in *Millimeter and Submillimeter Detectors for Astronomy*, T. Phillips and J. Zmuidzinas, eds., *Proc. SPIE* **4855**, pp. 108–114, 2003.
12. L. Duband and B. Collaudin *Cryogenics* **39**, pp. 659–663, 1999.
13. D. Lemke, U. Groezinger, O. Krause, R. Rohloff, and R. Haberland in *Infrared Spaceborne Remote Sensing VII*, M. S. Scholl and B. F. Andresen, eds., *Proc. SPIE* **3759**, pp. 205–213, 1999.
14. O. Krause, D. Lemke, U. Groezinger, A. Boehm, H. Baumeister, and R. Rohloff in *Infrared Spaceborne Remote Sensing VIII*, M. Strojnik and B. F. Andresen, eds., *Proc. SPIE* **4131**, pp. 120–131, 2000.
15. L. Looney, W. Raab, A. Poglitsch, and N. Geis *ApJ* **597**, pp. 628–643, 2003.
16. E. Renotte, J.-M. Gillis, C. A. Jamar, P. Laport, T. Salée, and S. Crehay in *Infrared Spaceborne Remote Sensing VII*, M. S. Scholl and B. F. Andresen, eds., *Proc. SPIE* **3759**, pp. 189–204, 1999.
17. A. Poglitsch, C. Waelkens, and N. Geis in *Infrared Spaceborne Remote Sensing VII*, M. S. Scholl and B. F. Andresen, eds., *Proc. SPIE* **3759**, pp. 221–233, 1999.
18. G. J. Stacey, J. W. Beeman, E. E. Haller, N. Geis, A. Poglitsch, and M. Rumitz *Int J. IR & Millimeter Waves.* **13**, p. 1689, 1992.